Nanoscale

PAPER

View Article Online
View Journal | View Issue

Cite this: *Nanoscale*, 2025, **17**, 20982

Thermal conductivity of individual single-crystalline $F_{16}CuPc$ nanoribbons

Yue Wen,†[a] Jeongho Cho,†[b] Linfeng Yu,[c] Yi-Ming Zhao,[a] Jingxuan Wang,[a] Lei Shen,[a] Guangzhao Qin,[c] Seok Min Yoon,*[d] Jongwoo Lim*[b,e,f] and Sunmi Shin*[a]

Received 30th May 2025,
Accepted 7th August 2025

DOI: 10.1039/d5nr02286j

rsc.li/nanoscale

Organic semiconductors are widely used in flexible electronics, optoelectronic devices, and thermoelectric systems. Among them, copper hexadecafluorophthalocyanine ($F_{16}CuPc$), an n-type organic semiconductor, exhibits excellent chemical and thermal stability, making it suitable for a range of device applications. As device architectures scale down to the nanoscale, understanding the intrinsic thermal transport properties of such materials becomes critical for effective thermal management. In this work, we report the first thermal conductivity measurement of individual single-crystalline $F_{16}CuPc$ nanoribbons using a suspended thermometry platform. We integrated individual nanoribbons into our measurement platform and conducted temperature dependent measurements. The thermal conductivity trend indicates the crystalline status of the sample. All samples exhibit thermal conductivity values of nearly 0.3 W m^{-1} K^{-1} at room temperature, attributed to short phonon mean free paths and weak intermolecular interactions. Molecular dynamics simulations further support the experimental trends and reveal anisotropic thermal transport characteristics. These results provide valuable insights into heat conduction mechanisms in small-molecule organic semiconductors and offer guidance for thermal design in future nanoscale device integration.

Introduction

Organic semiconductors have gained increasing interest owing to their application in flexible and lightweight electronic devices including organic photovoltaics (OPVs), organic field-effect transistors (OFETs), and organic light-emitting diodes (OLEDs).[1–5] With continued device miniaturization and increasing power densities, effective thermal management has become essential to maintain device stability and prevent thermal degradation.[6,7] Despite their growing attention, the intrinsic thermal transport properties of organic semiconductors—particularly in the single-crystalline form—remain unexplored.

Among small-molecule organic semiconductors, copper hexadecafluorophthalocyanine ($F_{16}CuPc$) has emerged as an n-type semiconductor with high chemical and thermal stability.[8,9] $F_{16}CuPc$ can be synthesized in various morphologies, including thin films and substrate-aligned nanoribbons, offering versatility for device integration.[10,11] Recent studies have demonstrated the use of substrate-guided growth techniques to integrate $F_{16}CuPc$ into various microelectronic devices, enabling *in situ* fabrication with enhanced molecular alignment and improved device performance uniformity.[12–16] While $F_{16}CuPc$ has been employed in various applications, its integration into nanoscale devices demands a comprehensive understanding of its thermal properties to enable effective thermal management.

Thermal measurements of organic materials are typically conducted on bulk films or polycrystalline aggregates, where boundary scattering, disorder, and the influence of the substrate obscure their intrinsic transport behavior.[17,18] To address this, direct thermal measurements on isolated single crystals are essential but experimentally demanding: ultrathin organic crystals are fragile, difficult to handle on suspended microdevices, and require a sensitive thermometry platform.

[a]*Department of Mechanical Engineering, College of Design and Engineering, National University of Singapore, 117575, Singapore. E-mail: mpeshin@nus.edu.sg*
[b]*Department of Chemistry, College of Science, Seoul National University, 1 Gwanak-ro, Gwanak-gu, Seoul, 08826, Republic of Korea. E-mail: jwlim@snu.ac.kr*
[c]*State Key Laboratory of Advanced Design and Manufacturing Technology for Vehicle, College of Mechanical and Vehicle Engineering, Hunan University, Changsha, 410082, People's Republic of China*
[d]*Department of Chemistry, College of Natural Science, Gyeongsang National University, Jinju-si, Gyeongsangnam-do, 52828, Republic of Korea. E-mail: smyoon@gnu.ac.kr*
[e]*Institute of Applied Physics, Seoul National University, 1 Gwanak-ro, Gwanak-gu, Seoul 08826, Republic of Korea*
[f]*Institute for Battery Research Innovation, Seoul National University, 1 Gwanak-ro, Gwanak-gu, Seoul 08826, Republic of Korea*
†These authors contributed equally to the work.

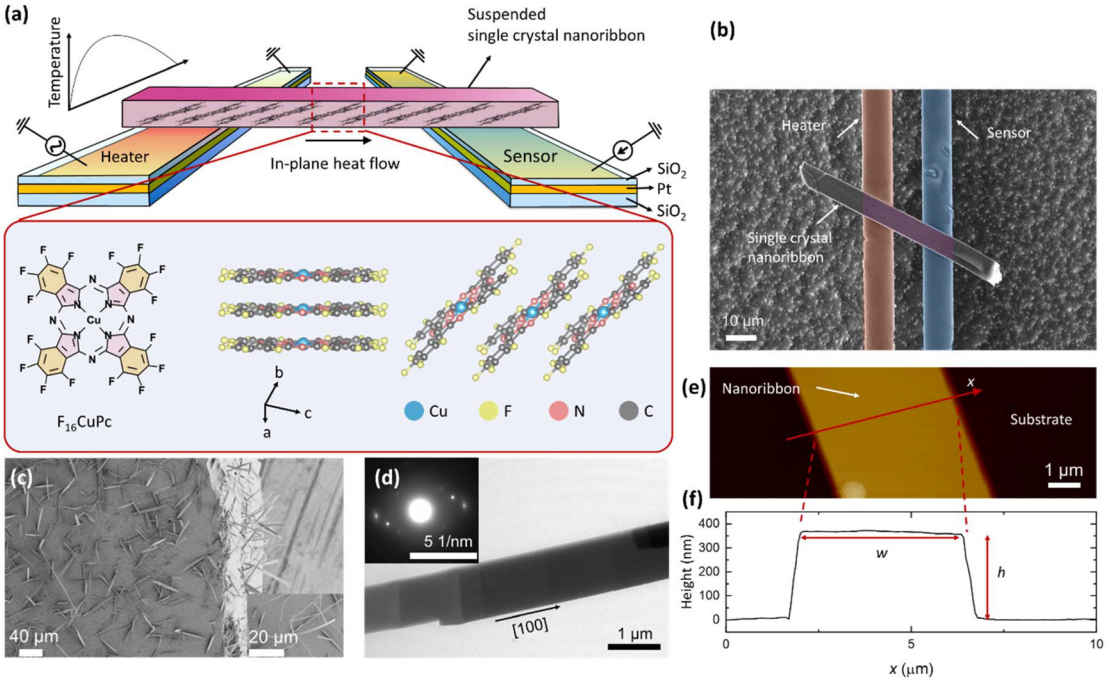

Fig. 1 (a) Schematic illustration of a single-crystalline $F_{16}CuPc$ nanoribbon sample integrated into our suspended measurement platform. (b) SEM image of the $F_{16}CuPc$ nanoribbon on our suspended device. (c) SEM image of the as-grown $F_{16}CuPc$ nanoribbon on the supporting substrate. The inset is the magnified view. (d) TEM image of the $F_{16}CuPc$ nanoribbon. The inset shows the corresponding SAED pattern. (e) AFM image of a section of the nanoribbon. (f) Height profile along the marked direction.

In this work, we demonstrate the thermal conductivity measurement of individual single-crystalline $F_{16}CuPc$ nanoribbons using a suspended thermal bridge setup (Fig. 1). By carefully transferring the pristine ribbons to the device and retrieving them for post-measurement characterization, we preserved their crystalline integrity and observed their temperature dependent thermal transport behavior. In addition to the experimental measurements, molecular dynamics (MD) simulations were carried out to elucidate phonon transport mechanisms and quantify the role of anisotropy. This work represents one of the first direct determinations of thermal conductivity in single-crystalline organic nanostructures and offers new insights into thermal transport in organic semiconductors.

Experimental

To obtain single-crystalline $F_{16}CuPc$ nanoribbons, $F_{16}CuPc$ powder (Aldrich, 80%) was purified by vacuum sublimation prior to use. A total of 0.04 g of the purified $F_{16}CuPc$ powder was placed in a ceramic boat, which was subsequently positioned at the center of a single-zone tube furnace. A precleaned Si(100) substrate was placed near the downstream end inside the quartz tube. Prior to heating, the tube was thoroughly purged with argon gas to eliminate residual ambient gases. The growth of $F_{16}CuPc$ nanoribbons was carried out at a substrate temperature of 360 °C, while the powder was heated to 500 °C at a ramping rate of 1.05 °C s^{-1}. The process was maintained for 40 minutes under an argon atmosphere with a flow rate of 100 sccm, yielding ribbons 1–10 μm wide and up to 500 μm long.[11] Fig. 1(c) shows the SEM image of the morphology of $F_{16}CuPc$ nanoribbons on Si (100). To analyze the structure of the as-grown $F_{16}CuPc$ ribbons, TEM was performed on the samples, and the corresponding SAED pattern was obtained, as shown in Fig. 1(d). The diffraction pattern confirms the crystalline status of $F_{16}CuPc$, with the [100] direction identified as the molecular stacking axis, corresponding to the *a*-axis.[19,20] The AFM image and height profile of the cross-section of the $F_{16}CuPc$ are shown in Fig. 1(e and f). The cross section is well defined and can be accurately determined, enabling calculation of thermal conductivity from the measured thermal conductance. Detailed information on sample dimensions is provided in the SI section 'Dimensions of $F_{16}CuPc$ Nanoribbon'.

To perform the thermal measurement, individual nanoribbons need to be picked out and integrated into our suspended thermal bridge setup. Fig. 1(a) provides an overview of the experimental setup. A single-crystalline $F_{16}CuPc$ nanoribbon is bridged between two suspended electrodes. An alternating current (AC) is applied to one electrode to induce Joule heating, while the resulting temperature rise is detected at the sensing electrode. This configuration enables direct measurement of the thermal conductance of the nanoribbon.[21]

Due to the high electrical conductivity of the $F_{16}CuPc$ nanoribbon, appropriate electrical insulation is required to prevent current leakage and ensure accurate thermal

measurements.[22–25] We developed a measurement platform that provided the necessary electrical insulation while maintaining access to external circuit connections (Fig. 2(a)). The fabrication process began with a SiO_2/Si substrate. Electrodes were first patterned using photolithography, followed by the deposition of Ti/Pt. A 100 nm-thick SiO_2 insulating layer was then deposited over the entire device, including the electrodes. Subsequently, a second photolithography step was used to define the "window" region where the silicon would later be etched to create the suspended structure. In this step, the SiO_2 layer within the window was selectively removed to expose the underlying Si substrate, while the electrodes and the SiO_2 insulating layer covering them remained protected. A third photolithography step was then carried out to open the metal contact pads by removing the SiO_2 layer above them, allowing electrical connection to the external circuit. Finally, XeF_2 vapor etching was used to isotropically remove the exposed silicon beneath the "window" area, releasing the beams and forming the suspended structure.

Individual F_{16}CuPc nanoribbons were transferred onto the custom-fabricated suspended devices using a tungsten micromanipulator tip, which was carried out under an optical microscope. The tip was gently scraped across the growth substrate to detach nanoribbons, and the process was repeated until a suitable ribbon – intact and with dimensions compatible with the device – was selected. The chosen nanoribbon was then aligned across the suspended beams of the device. To improve thermal contact, a small drop of isopropyl alcohol (IPA) was applied to the contact region.[26,27] The tungsten tip was then brought into proximity with the device until the nanoribbon made contact with both beams, after which the tip was carefully withdrawn to complete the sample placement and integration process (Fig. 2(d and e)). Sample dimensions were determined after the thermal measurement to avoid destruction of the crystalline structure.

Results and discussion

Fig. 3(a) illustrates the measurement circuitry used in our setup. The measurement was conducted in a high-vacuum cryostat chamber ($<10^{-6}$ mbar). An AC was applied to the heating beam, and the resulting temperature rise is correlated with the temperature coefficient of resistance (TCR) of the Pt electrode, as described by eqn (1). The temperature rise induces a third harmonic voltage response, which is detected using a lock-in amplifier (Stanford Research SR830) – this technique is known as the three-omega (3ω) method. Heat is conducted through the sample to the sensing side. On the sensing side, we used a Wheatstone bridge circuit to improve the

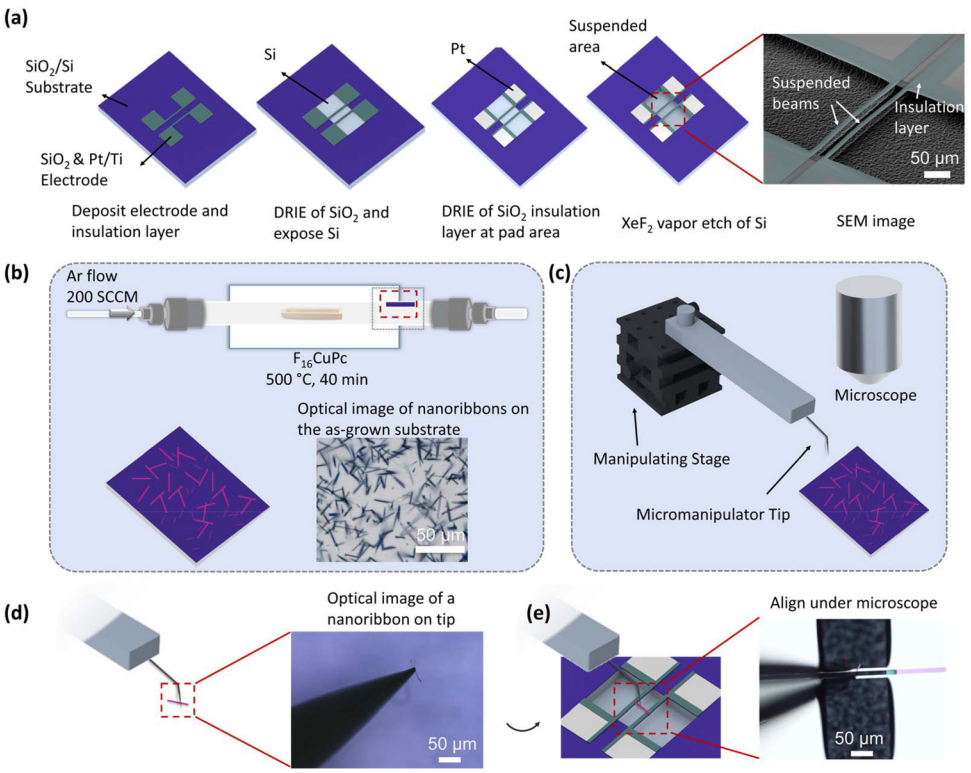

Fig. 2 (a) Illustration of the fabrication sequence of the insulated suspended thermometry device and a SEM image of the completed device. (b) Schematic of the synthesis process and the substrate with grown F_{16}CuPc nanoribbons, and an optical image showing a section of the substrate. (c) Setup of the customized transfer stage, including the micromanipulator and optical microscope. (d) Illustration of a picked up individual F_{16}CuPc nanoribbon with a micromanipulator tip and the optical image. (e) Plot of the nanoribbon being aligned and brought into contact with the suspended device and the optical image.

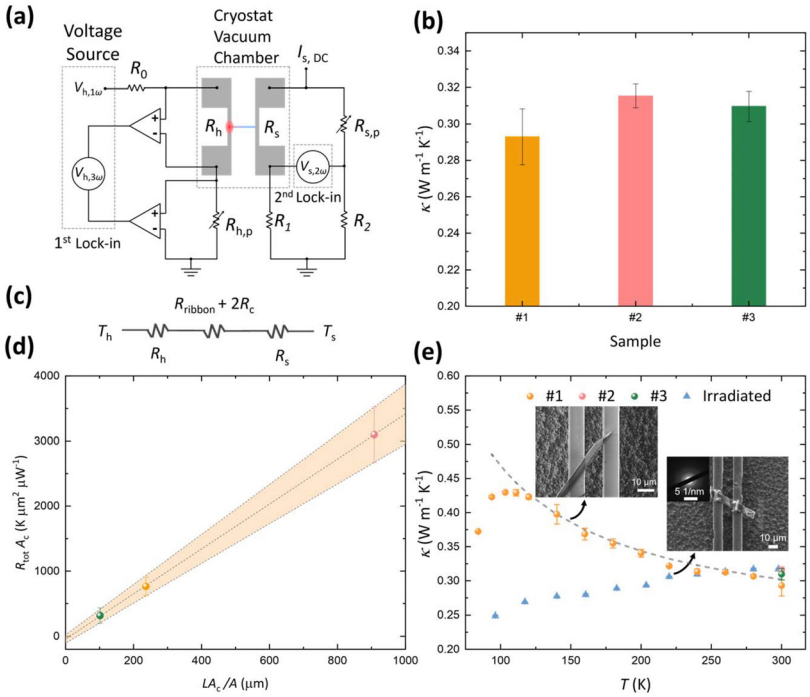

Fig. 3 (a) Illustration of an AC-modulated thermometry platform with a cryostat vacuum chamber. (b) Plot of thermal conductivity measured at room temperature for sample #1, sample #2, and sample #3. (c) Thermal resistance circuit. (d) Linear fit of $R_{tot}{\cdot}A_c$ *versus* $L/A{\cdot}A_c$ to extract the range of specific contact resistance with nanoribbons with similar thermal conductivity values at room temperature. Here, L is the suspended length between the heater and the sensor, and A is the cross-sectional area of the nanoribbon. (e) Temperature-dependent thermal conductivity of crystalline and amorphous-like $F_{16}CuPc$ samples. The dashed gray line represents $1/T$ temperature dependence. Insets show SEM images of sample #1 and sample #4, with the SAED pattern of sample #4 indicating the loss of the crystalline structure.

measurement sensitivity, and the voltage signal was picked up using the lock-in amplifier with an applied direct current (DC) (eqn (2)).[28,29]

$$\Delta T_h = 3\frac{V_{h,3\omega}}{I_\omega}\left(\frac{dR_h}{dT}\right)^{-1} \quad (1)$$

$$\Delta T_s = \sqrt{2}\frac{V_{s,2\omega}(R_s + R_{s,p} + R_1 + R_2)}{I_{dc}R_2}\left(\frac{dR_s}{dT}\right)^{-1} \quad (2)$$

To examine the influence of contact thermal resistance we conducted measurement for three samples with different cross-sectional areas and suspended lengths. First, these samples exhibit similar thermal conductivity at room temperature as shown in Fig. 3(b). According to the equivalent thermal resistance circuit shown in Fig. 3(c), the total resistance (R_{tot}) would show a linear relationship with the thermal resistance of the suspended samples as depicted in eqn (3),[30]

$$R_{tot} = R_{ribbon} + 2R_c \quad (3)$$

where

$$R_{ribbon} = \frac{l}{\kappa A}, R_c = \frac{r_c}{A_c}. \quad (4)$$

Here, l is the sample length, k is the thermal conductivity, A is the cross-sectional area, r_c is the specific contact resistance, and A_c is the contact area. We assumed a constant specific contact resistance across all samples, given the consistent fabrication and electrode interface conditions.[31] We performed a linear fit of $R_{tot}{\cdot}A_c$ *versus* $l/A{\cdot}A_c$. The extrapolated intercept corresponds to $2r_c$, from which we obtained a maximum specific contact resistance r_c of 21.1 K μW^{-1} μm^2. This yields a total contact resistance of 2.9 K μW^{-1}, contributing at most 6.6% to the total measured resistance. This indicates that the reported thermal conductivity represents a conservative lower bound. It is worth emphasizing that the nanoribbon adheres well to the beams following IPA-assisted transfer, and the relatively low thermal conductivity ensures that the sample resistance dominates the overall thermal resistance. These observations collectively suggest that contact resistance has minimal influence on the measurement results.[32,33]

During our measurements, we found that the suspended SiO_2 beams exhibit measurable heat conductance in the form of radiative heat transfer. This contribution increases with temperature and is most prominent at 300 K, the upper bound temperature in our measurement range.[30] Therefore, to accurately reflect the actual sample conductance, the background conductance is subtracted from the total measured conductance. The thermal conductivity values of the three samples with varying dimensions at room temperature are presented in Fig. 3(b), after subtracting background conductance based on the analysis described in the SI section 'Background Conductance'. All samples exhibit consistent values in the

range of 0.29–0.32 W m^{-1} K^{-1}, with variations falling within experimental uncertainty. The relatively low κ values at room temperature imply short phonon mean free paths, consistent with the presence of weak intermolecular interactions that suppress long-propagating phonons. The similarity in κ across samples ranging from 5.6 to 17.2 μm indicates diffusive transport, where the phonon mean free path is on the order of tens of nanometers and much smaller than the sample length, suggesting that heat conduction is dominated by intrinsic phonon scattering rather than boundary or size effects.[34]

To further investigate the crystalline properties of the samples, we conducted temperature dependent thermal conductivity measurements. Fig. 3(e) presents the temperature dependent thermal conductivity values of two F_{16}CuPc nanoribbon samples. For sample #1, it displays a peak in thermal conductivity near 100 K and a gradual decrease that approximately follows $1/T$ dependence at higher temperatures. This behavior is understood as the anharmonic phonon scattering in crystal materials where phonon interactions increase with temperature and limit thermal transport.[33,35] The presence of such a peak is a distinctive feature of crystalline materials with reduced phonon–phonon scattering at low temperatures.

To confirm that the observed temperature dependent trend originated from the crystalline status of the sample, we performed the same measurements on a sample that was subjected to ion beam irradiation for comparison. It is known that prolonged ion beam exposure induces structural damage in organic materials.[36] Accordingly, we processed one of the samples (irradiated) using focused ion beam (FIB) to disrupt its crystalline order and the irradiated sample exhibits clearly different thermal transport behavior. Its thermal conductivity increases monotonically from 100 K to 300 K, with no discernible peak, and reaches approximately 0.32 W m^{-1} K^{-1} at room temperature. The absence of a peak in the temperature dependent trend and the suppressed thermal conductivity at low temperatures suggest that the sample has transitioned to an amorphous-like phase, due to structural damage induced by ion beam exposure.[27,37,38] This damage introduces point defects and disrupts molecular ordering, significantly impeding phonon propagation and resulting in enhanced defect scattering. Notably, the thermal conductivity of all samples converges to a low value around 0.3 W m^{-1} K^{-1} which is attributed to several reasons. First, high-energy phonon–phonon Umklapp scattering dominates at this temperature, shortening phonon lifetimes so that κ is governed by these strongly scattered phonons. Second, the weak van der Waals interactions that bind F_{16}CuPc molecular layers intrinsically suppress heat flow, setting a low upper bound on thermal conductivity even for defect-free crystals. Finally, once higher energy phonon scattering has reduced phonon mean free paths to tens of nanometers, additional disorder from ion-beam damage has little further effect. Our measurement represents the first effort to determine the thermal conductivity of single-crystalline F_{16}CuPc nanoribbons and reveals the impact of ion beam exposure on the sample morphology, which leads to a distinctly altered thermal transport behavior.

To better understand the measured thermal conductivity values, we performed molecular dynamics (MD) simulation for F_{16}CuPc and observed the thermal transport properties. The empirical potentials similar to that obtained by Tersoff *et al.* do not work for such a complex system with four different elements.[39] Here, we employed a single neural network ML framework to train the neuroevolution potential (NEP) developed by Fan *et al.*[40] The machine learning potential is trained based on the DFT calculated energy and force data implemented using GPUMD to achieve more reliable MD simulation.[41] The DFT data are calculated using the Vienna *Ab initio* Simulation Package (VASP)[42] through the *ab initio* Molecular Dynamics (AIMD) simulation. During the MD simulation for thermal transport behavior, the DFT-D3 van der Waals interaction is included to describe the long range forces within 12 Å more accurately.[43] With the NEP, the thermal conductivity of EMD can be calculated using the Green–Kubo formula:

$$\kappa(t) = \frac{V}{3k_B T^2} \sum_{\alpha=1}^{3} \int_0^t \mathrm{d}t' \langle J(0) J(t') \rangle, \quad (5)$$

where k_B, V, and T are the Boltzmann constant, the volume and the temperature. $J(0)J(t')$ represents the heat current J autocorrelation function for the associated time t'.

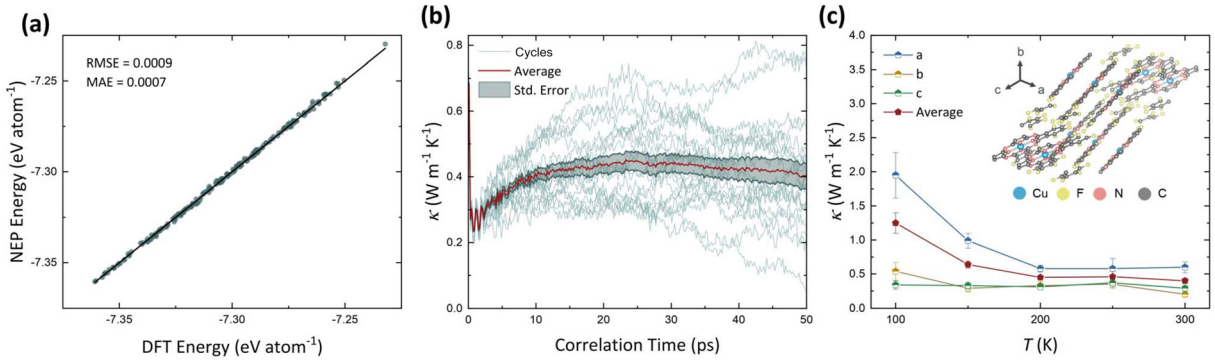

Fig. 4 (a) The comparison between predicted energy by machine learning potential and DFT calculated energy. (b) The thermal conductivity run during the EMD process. (c) The thermal conductivity at different temperatures calculated from the EMD process.

The trained potential accurately predicts the energy of a test set, which agrees well with the DFT calculated energy as shown in Fig. 4(a). Based on this reliable potential, we ran the equilibrium molecular dynamics (EMD) simulation to calculate the thermal conductivity of the bulk structure by solving the Green–Kubo formula.[44] The average thermal conductivity regardless of the transport directions reaches 0.40 W m^{-1} K^{-1} at 300 K from the EMD process in Fig. 4(b). The simulated thermal conductivity shows good agreement with the experimental result, although it slightly overestimates the measured value. This is reasonable given that the simulation assumes a perfect crystal, while the samples obtained in experiments may contain defects that introduce additional phonon scattering.[34] We then ran the EMD calculations for the temperature range from 100 K to 300 K and obtained the thermal conductivity values as shown in Fig. 4(c). The average thermal conductivity decreases with increasing temperature within this range, consistent with our experimental observations of the temperature dependent trend in the crystalline sample. The thermal conductivity along different crystallographic axes is also modelled to provide further insight into the anisotropy of thermal transport of F_{16}CuPc. Anisotropy is evident from the modelling results, with thermal conductivity along the *a*-axis exhibiting more pronounced temperature dependence. Since the molecular stacking occurs along the *a*-axis, our measurements are expected to predominantly reveal transport along this direction. The deviation observed at lower temperatures can be attributed to the reduced thermal resistance of the sample in this regime, which makes the contribution from contact resistance relatively more noticeable. Overall, the MD simulations support our measured values and offer additional insight into the anisotropic thermal transport properties of this material.

Conclusions

In this work, we report the first direct thermal conductivity measurements of individual single-crystalline F_{16}CuPc nanoribbons. We carefully transferred individual F_{16}CuPc nanoribbons onto a sensitive suspended thermometry platform while preserving their crystalline structure. The temperature dependent thermal transport behavior reveals their crystalline status. In contrast, nanoribbons subjected to ion exposure exhibited amorphous-like characteristics. The crystalline sample showed increasing thermal conductivity with decreasing temperature, with a peak near 100 K, consistent with the reduced effect of phonon–phonon scattering at low temperatures. The ion beam exposed samples display monotonic temperature dependence, indicating amorphous-like behavior and increased defect scattering.

The thermal conductivity across all measured samples at room temperature converges to approximately 0.3 W m^{-1} K^{-1}, which is attributed to the short phonon mean free paths and the inherently weak van der Waals interactions in the material. Molecular dynamics simulations support the observed temperature dependent trends. This relatively low thermal conductivity has two important implications for device applications. On the one hand, it highlights the need for careful thermal management when integrating F_{16}CuPc into active components such as organic field-effect transistors, organic photovoltaics, or large-area photodetectors, where localized heating may degrade performance and reliability. On the other hand, the same low k value makes F_{16}CuPc an ideal material for thermal insulation layers in nanoscale and flexible electronics, where thermal isolation between densely packed components is crucial. Therefore, understanding and quantifying its thermal behavior is essential for both performance optimization and thermal design in emerging organic electronic platforms.

Author contributions

Y. W., J. C., J. L., and S. S. devised the experimental designs. Y. W., J. C., S. M. Y., and J. W. prepared the samples. Y. W. conducted the thermal measurement. L. Y. and Y.-M. Z. conducted the molecular dynamics modeling. All authors discussed the results and wrote the manuscript.

Conflicts of interest

There is no conflicts to declare.

Data availability

The data supporting this study have been included in the article and in the SI.

Supplementary information is available. The dimensions of measured samples, method for obtaining the thermal conductivity and details of length dependent MD modeling. See DOI: **https://doi.org/10.1039/d5nr02286j**.

Acknowledgements

The authors acknowledge the support from Singapore Ministry of Education academic research fund tier 1 (A-8002147-00-00). This work was also supported by the Technology Innovation Program (RS-2024-00400766) funded by the Ministry of Trade, Industry and Energy (MOTIE, Korea). Y.-M. Z. gratefully acknowledges the support of China Scholarship Council (No. CSC202104910079). J. C., S. M. Y., and J. L. acknowledge the financial support from Samsung Electronics.

References

1 S. R. Forrest, *Nature*, 2004, **428**, 911–918.
2 S. Liu, W. M. Wang, A. L. Briseno, S. C. Mannsfeld and Z. Bao, *Adv. Mater.*, 2009, **21**, 1217–1232.

3 H.-Y. Chen, J. Hou, S. Zhang, Y. Liang, G. Yang, Y. Yang, L. Yu, Y. Wu and G. Li, *Nat. Photonics*, 2009, **3**, 649–653.
4 Y. Qian, X. Zhang, L. Xie, D. Qi, B. K. Chandran, X. Chen and W. Huang, *Adv. Mater.*, 2016, **28**, 9243–9265.
5 S. S. Swayamprabha, D. K. Dubey, Shahnawaz, R. A. K. Yadav, M. R. Nagar, A. Sharma, F. C. Tung and J. H. Jou, *Adv. Sci.*, 2021, **8**, 2002254.
6 E. Pop, *Nano Res.*, 2010, **3**, 147–169.
7 D. G. Cahill, P. V. Braun, G. Chen, D. R. Clarke, S. Fan, K. E. Goodson, P. Keblinski, W. P. King, G. D. Mahan and A. Majumdar, *Appl. Phys. Rev.*, 2014, **1**, 011305.
8 Z. Bao, A. J. Lovinger and J. Brown, *J. Am. Chem. Soc.*, 1998, **120**, 207–208.
9 J. Wang, H. Wang, X. Yan, H. Huang, D. Jin, J. Shi, Y. Tang and D. Yan, *Adv. Funct. Mater.*, 2006, **16**, 824–830.
10 W. Chen, S. Chen, S. Chen, Y. Li Huang, H. Huang, D. C. Qi, X. Y. Gao, J. Ma and A. T. S. Wee, *J. Appl. Phys.*, 2009, **106**, 064910.
11 S. M. Yoon, H. J. Song, I.-C. Hwang, K. S. Kim and H. C. Choi, *Chem. Commun.*, 2010, **46**, 231–233.
12 S. M. Yoon, S. J. Lou, S. Loser, J. Smith, L. X. Chen, A. Facchetti and T. Marks, *Nano Lett.*, 2012, **12**, 6315–6321.
13 G. Pindolia, J. Pandya, S. Shinde and P. K. Jha, *Int. J. Energy Res.*, 2022, **46**, 15127–15142.
14 C. Yoon, Y. Zhou, Z. C. Wang and A. Dodabalapur, *Appl. Phys. Lett.*, 2024, **125**, 123502.
15 L. Zhang, X. Wang, W. Zhou, H. Wang, J. Song, Z. Zhao, J. Liao, J. Song, Y. Li and J. Xu, *Nano Res.*, 2023, **16**, 9561–9568.
16 X. Chen, W. Mao, W. Zhou, P. Huang, H. Liu, X. Wang, Z. Liang, Q. Yang, Y. Chen and G. Zhou, *ACS Appl. Mater. Interfaces*, 2024, **16**, 57512–57523.
17 G. Ren, Z. Wang, X. Huang, D. Hur, M. A. Pfeifer, M. N. Silberstein and Z. Tian, *Mater. Horiz.*, 2025, 2957–2964.
18 X. Rodríguez-Martínez, F. Saiz, B. Dörling, S. Marina, J. Guo, K. Xu, H. Chen, J. Martin, I. McCulloch and R. Rurali, *Adv. Energy Mater.*, 2024, **14**, 2401705.
19 Y. Zhang, H. Dong, Q. Tang, S. Ferdous, F. Liu, S. C. Mannsfeld, W. Hu and A. L. Briseno, *J. Am. Chem. Soc.*, 2010, **132**, 11580–11584.
20 H. Jiang, J. Ye, P. Hu, F. Wei, K. Du, N. Wang, T. Ba, S. Feng and C. Kloc, *Sci. Rep.*, 2014, **4**, 7573.
21 L. Shi, D. Li, C. Yu, W. Jang, D. Kim, Z. Yao, P. Kim and A. Majumdar, *J. Heat Transfer*, 2003, **125**, 881–888.
22 K. Lau, J. Tang, H. Sun, C. Lee, S. Lee and D. Yan, *Appl. Phys. Lett.*, 2006, **88**, 173513.
23 E. Kol'tsov, T. Basova, P. Semyannikov and I. Igumenov, *Mater. Chem. Phys.*, 2004, **86**, 222–227.
24 J. Park, S. Cho, S. Park, J. Jeong, H. Kim, Y. Yi and M.-H. Cho, *Synth. Met.*, 2010, **160**, 108–112.
25 S. Li, R. E. Simpson and S. Shin, *Nanoscale*, 2023, **15**, 15965–15974.
26 R. Shrestha, P. Li, B. Chatterjee, T. Zheng, X. Wu, Z. Liu, T. Luo, S. Choi, K. Hippalgaonkar and M. P. De Boer, *Nat. Commun.*, 2018, **9**, 1664.
27 R. Shrestha, Y. Luan, X. Luo, S. Shin, T. Zhang, P. Smith, W. Gong, M. Bockstaller, T. Luo and R. Chen, *Nat. Commun.*, 2020, **11**, 4346.
28 J. Zheng, M. C. Wingert, J. Moon and R. Chen, *Semicond. Sci. Technol.*, 2016, **31**, 084005.
29 J. Zheng, M. C. Wingert, E. Dechaumphai and R. Chen, *Rev. Sci. Instrum.*, 2013, **84**, 114901.
30 J. Wang, Y. Wen, D. Pan, S. Lin, A. Chinnappan, Q. He, C. Liu, Z. Huang, S. Cai and S. Ramakrishna, *Nano Lett.*, 2024, **24**, 9990–9997.
31 C. Yu, S. Saha, J. Zhou, L. Shi, A. M. Cassell, B. A. Cruden, Q. Ngo and J. Li, *J. Heat Transfer*, 2006, **128**, 234–239.
32 Z. Zhong, M. C. Wingert, J. Strzalka, H.-H. Wang, T. Sun, J. Wang, R. Chen and Z. Jiang, *Nanoscale*, 2014, **6**, 8283–8291.
33 J. Ma, Q. Zhang, A. Mayo, Z. Ni, H. Yi, Y. Chen, R. Mu, L. M. Bellan and D. Li, *Nanoscale*, 2015, **7**, 16899–16908.
34 C. Shao, Y. Jin, K. Pipe, M. Shtein and J. Kieffer, *J. Phys. Chem. C*, 2014, **118**, 9861–9870.
35 V. Singh, T. L. Bougher, A. Weathers, Y. Cai, K. Bi, M. T. Pettes, S. A. Mcmenamin, W. Lv, D. P. Resler, T. R. Gattuso, D. H. Altman, K. H. Sandhage, L. Shi, A. Henry and B. A. Cola, *Nat. Nanotechnol.*, 2014, **9**, 384–390.
36 N. Bassim, B. De Gregorio, A. Kilcoyne, K. Scott, T. Chou, S. Wirick, G. Cody and R. Stroud, *J. Microsc.*, 2012, **245**, 288–301.
37 A. Aiyiti, S. Hu, C. Wang, Q. Xi, Z. Cheng, M. Xia, Y. Ma, J. Wu, J. Guo and Q. Wang, *Nanoscale*, 2018, **10**, 2727–2734.
38 Y. Zhao, M. Zheng, J. Wu, X. Guan, A. Suwardi, Y. Li, M. Lal, G. Xie, G. Zhang and L. Zhang, *Nanoscale*, 2021, **13**, 11561–11567.
39 J. Tersoff, *Phys. Rev. B: Condens. Matter Mater. Phys.*, 1989, **39**, 5566.
40 Z. Fan, Z. Zeng, C. Zhang, Y. Wang, K. Song, H. Dong, Y. Chen and T. Ala-Nissila, *Phys. Rev. B*, 2021, **104**, 104309.
41 Z. Fan, W. Chen, V. Vierimaa and A. Harju, *Comput. Phys. Commun.*, 2017, **218**, 10–16.
42 G. Kresse and J. Furthmüller, *Phys. Rev. B: Condens. Matter Mater. Phys.*, 1996, **54**, 11169.
43 S. Grimme, J. Antony, S. Ehrlich and H. Krieg, *J. Chem. Phys.*, 2010, **132**, 154104.
44 Z. Fan, L. F. C. Pereira, P. Hirvonen, M. M. Ervasti, K. R. Elder, D. Donadio, T. Ala-Nissila and A. Harju, *Phys. Rev. B*, 2017, **95**, 144309.